PHYSICAL REVIEW MATERIALS **2**, 085408 (2018)

Lithiation properties of sp^2 carbon allotropes

Aurélien Lherbier,[1,*] Gil Vander Marcken,[1] Benoît Van Troeye,[1] Andrés Rafael Botello-Méndez,[1,2] Jean-Joseph Adjizian,[1]
Geoffroy Hautier,[1] Xavier Gonze,[1] Gian-Marco Rignanese,[1] and Jean-Christophe Charlier[1]
[1]*Université catholique de Louvain, Institute of Condensed Matter and Nanosciences, Chemin des étoiles 8, 1348 Louvain-la-Neuve, Belgium*
[2]*Universidad Nacional Autónoma de México, Institute of Physics, 20-364, 01000 México, D.F., Mexico*

(Received 9 May 2018; published 29 August 2018)

Increasing the storage capacity of lithium electrodes, without altering their cyclability, is one of the key challenges for modern ion-based batteries. For graphite-based anodes, the well-known capacity limit is ~370 mAh/g, which corresponds to a lithium composition of Li_1C_6. Lithium intercalation is accompanied by a volume expansion of ~10%. In the present work, accurate first-principles methods are used to investigate the performance of different bulk sp^2 carbon allotropes as anodes in lithium-ion batteries. Compared to graphite, which is an alternated stack of graphene layers (Bernal stacking) exhibiting a perfect hexagonal tiling, the layers of the other stacked systems considered are constructed from various polygonal carbon rings, such as squares, pentagons, hexagons, heptagons, octagons, and dodecagons. These sp^2 allotropes, which appear locally in defective graphene and grain boundaries, can exhibit a substantial increase in specific capacity with respect to graphite (up to a factor of two, i.e., Li_2C_6) with only a relatively small volume expansion (at most 25%). The mechanisms for this predicted increase in the number of lithium atoms that can be hosted in these still hypothetical carbon crystals are analyzed in detail, yielding global strategies for improving lithium capacity in sp^2 carbon-based batteries. In addition, these results offer an insight on the local mechanism of Li incorporation in randomly defective graphite.

DOI: 10.1103/PhysRevMaterials.2.085408

I. INTRODUCTION

Graphite is known to be a reliable choice of electrode for Li-ion batteries [1]. The first carbon anode for such batteries was initially created using pyrolitic graphite in the late 1980s [2]. The most important reasons for choosing an sp^2 carbon layered material are its excellent cyclability, its high Coulombic efficiency, and its good structural stability, which preserves the integrity of the material after many lithiation/delithiation cycles (charge only induces a ~10% volume expansion which can be endured mechanically by graphite). However, the limiting factor for modern technologies [3] based on carbon derives from the relatively poor Li storage capacity of Li_1C_6, which translates into a gravimetric capacity of 372.2 mAh/g. This is to be compared for instance to about 3000–4000 mA h/g for silicon albeit with a volumetric expansion up to 300% [4,5].

Modifying the local chemistry of the otherwise perfect carbon honeycomb lattice can yield to a substantial increase in Li storage capacity. This has been previously demonstrated for boron-doped graphite [6–11] and carbon nanotubes [12]. Intentional nitrogen doping can also be effective if the latter comes with the creation of vacancies, thus forming vacancy-nitrogen complexes that act as acceptors (pyridinic and pyrrolic nitrogen) [10,13]. While pristine monolayer graphene cannot store Li at all [14–17], incorporating structural defects has been suggested to increase Li storage capacity of monolayer graphene [15,17,18] up to $Li_{4.5}C_6$ and Li_3C_6 for a large amount of divacancies and Stone-Thrower-Wales defects, respectively [17]. Incorporating nonhexagonal rings in the carbon honeycomb lattice is thus a possible strategy for improving the storage capacity [19], which was also demonstrated experimentally with few layers of defective graphene sheets [20–23]. It has been observed that defects can be created during its synthesis or intentionally produced [24,25]. However, it is difficult to control the incorporation of structural defects, which can thus possibly lead to highly and randomly defective graphene or even an *amorphous* graphene structure. This limits its use in the design of efficient anodes for Li-ion batteries application. In contrast, 2D carbon allotropes that contain a perfect periodic arrangement of nonhexagonal rings in their crystalline structure have to be considered. Many of these structures have been imagined over the past decades [26], varying the tiling with squares, pentagons, hexagons, heptagons, and octagons but trying to preserve the sp^2 character of the carbon-carbon bond [27–32]. All these allotropes are found to be metastable compared to graphene. However, several insights towards a possible bottom-up chemical synthesis have been reported in the literature. For instance, the uniaxial self-assembly of biphenylene monomers has demonstrated the possibility of creating 1D nanoribbons containing squares, hexagons, and octagons thus opening the road towards the 2D layer synthesis [33]. A similar strategy may be followed to achieve the synthesis of many other sp^2 carbon systems with various polygonal forms. Other examples of monolayer or bilayer carbon-based crystalline structures involving sp bonding and more porous networks such as the experimentally synthesized graphyne [34] and graphdiyne [35] have also been investigated theoretically, suggesting an improved Li storage capacity.

Although for all of these alternative 2D carbon structures the gravimetric capacities are appreciably increased, the latter systems remain 2D in essence and their absolute capacities in practice are still rather small. Indeed, obtaining the mass

---

[*] Corresponding author: aurelien.lherbier@uclouvain.be

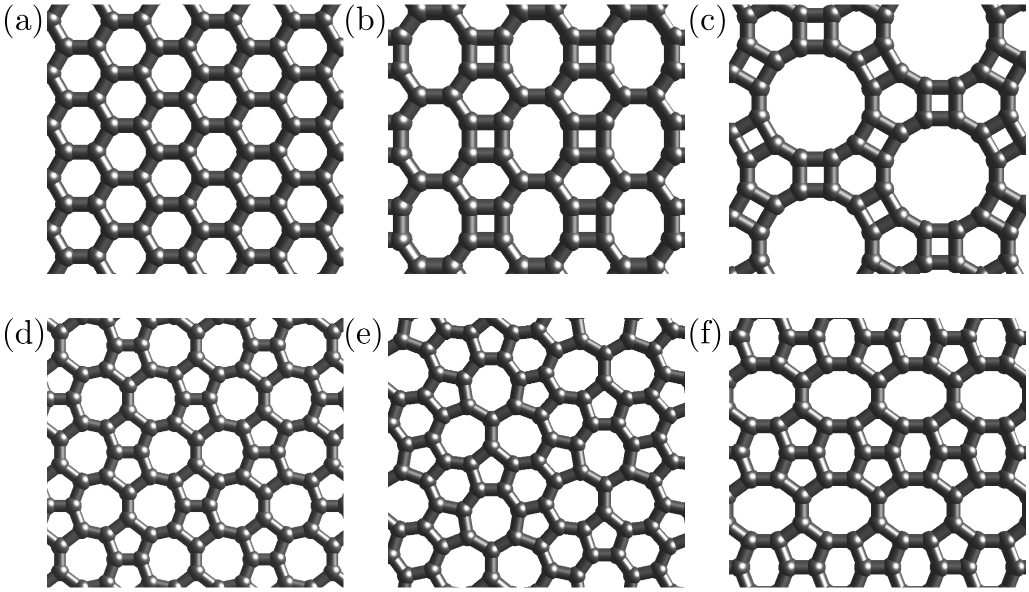

FIG. 1. Top view of the relaxed geometries of the different bulk sp^2 carbon allotropes considered for lithiation (only one layer is represented). From (a) to (f): graphite (6), tetrahexaoctite (4-6-8), tetrahexadodectite (4-6-12), pentaheptite (5-7), pentahexaheptite (5-6-7), and pentahexaoctite (5-6-8), respectively.

of a typical coin cell requires a surface of ~140 m^2 for an atomically thin anode battery [36]. It is therefore necessary to investigate the stacking of such not-yet-synthesized carbon layers to determine if the high Li storage capacities observed in mono- or bilayer systems still remain in the corresponding 3D bulk systems.

Recent progresses in the field of 2D materials, in particular for graphene, boron-nitride, and some transition metal dichalcogenides, have demonstrated the feasibility of stacking several 2D layers on top of each other, using transfer techniques and layer by layer deposition. Following this idea, known as van der Waals heterostructures [37], one could imagine building new "bulk" phases from their 2D counterparts. In parallel, the advances of the bottom-up chemistry [38] opens an interesting road to the synthesis of new 2D materials, in particular new 2D carbon allotropes. In some cases, the stacking can be obtained directly during the synthesis of the 2D layer systems by tuning the growth conditions. For instance, such an approach can yield to the formation of multilayered covalent organic frameworks (COFs) [39]. In fact, using appropriate monomer precursors, one could also produce metallic 2D covalent conjugated polymers (2DCPs) [40] with attractive electronic transport properties [41]. Although these approaches offer the possibility of scalability, in general they remain expensive and it is very important to know whether there is a gain in performance in such bulk sp^2 carbon allotropes. Density functional theory (DFT) allows one to answer this question, as it has been used to understand the lithiation of graphite including its different lithiation stages [42,43].

In the present article, five different bulk sp^2 carbon systems have been considered in addition to graphite, taken as the reference. These other sp^2 carbon layered systems depicted in Fig. 1 are structures which have not yet been synthesized experimentally, namely from (b) to (e), tetrahexaoctite (4-6-8) [29], tetrahexadodectite (4-6-12) [28], pentahexaheptite (5-6-7, also known as hexagonal Haeckelite) [27], pentahexaoctite (5-6-8) [32], and pentaheptite (5-7) [44], respectively. These six systems present a diversity in the polygonal carbon rings composition, varying from squares to dodecagons. The paper is organized as follows. Section II describes the computational methodology employed in this theoretical study. In Section III, the structural and electronic properties of the bulk sp^2 carbon allotropes are analyzed. In Sec. IV, the lithiation of our reference system, i.e., graphite, is analyzed. In Sec. V, the lithiation of all the other considered carbon systems is examined. Finally, the results are gathered and the perspectives of sp^2 carbon allotropes are discussed with respect to their potential as anodes in Li-ion-based batteries.

II. METHODS

First-principles simulations are employed to optimize atomic positions and cell geometries to compute total energies and electronic band structures of the various pristine and lithiated sp^2 carbon bulk layered systems. Calculations are performed using the self-consistent DFT method as implemented in the VASP package [45,46]. The exchange-correlation energy is described using the nonlocal optB86b-vdW functional [47–50] to account properly for van der Waals (vdW) interactions and, in the present case, long range electron-electron correlations between planes [51,52]. The projector augmented wave (PAW) method [53,54] is used and the pseudopotentials chosen accordingly. The plane-wave energy cutoff was set to 1000 eV (36.75 Ha). The atomic positions are relaxed until the forces on each atom are less than 0.01 eV/Å and the cell geometries are optimized. The spin degree of freedom is not accounted for in the calculations since we do not expect it to play any role in the present framework. The Monkhorst-Pack [55] k-point grids are determined automatically from pymatgen tools [56] by imposing densities ranging from 660 to 1400 k points per Å^{-3}. Bader analysis [57,58] is used to investigate

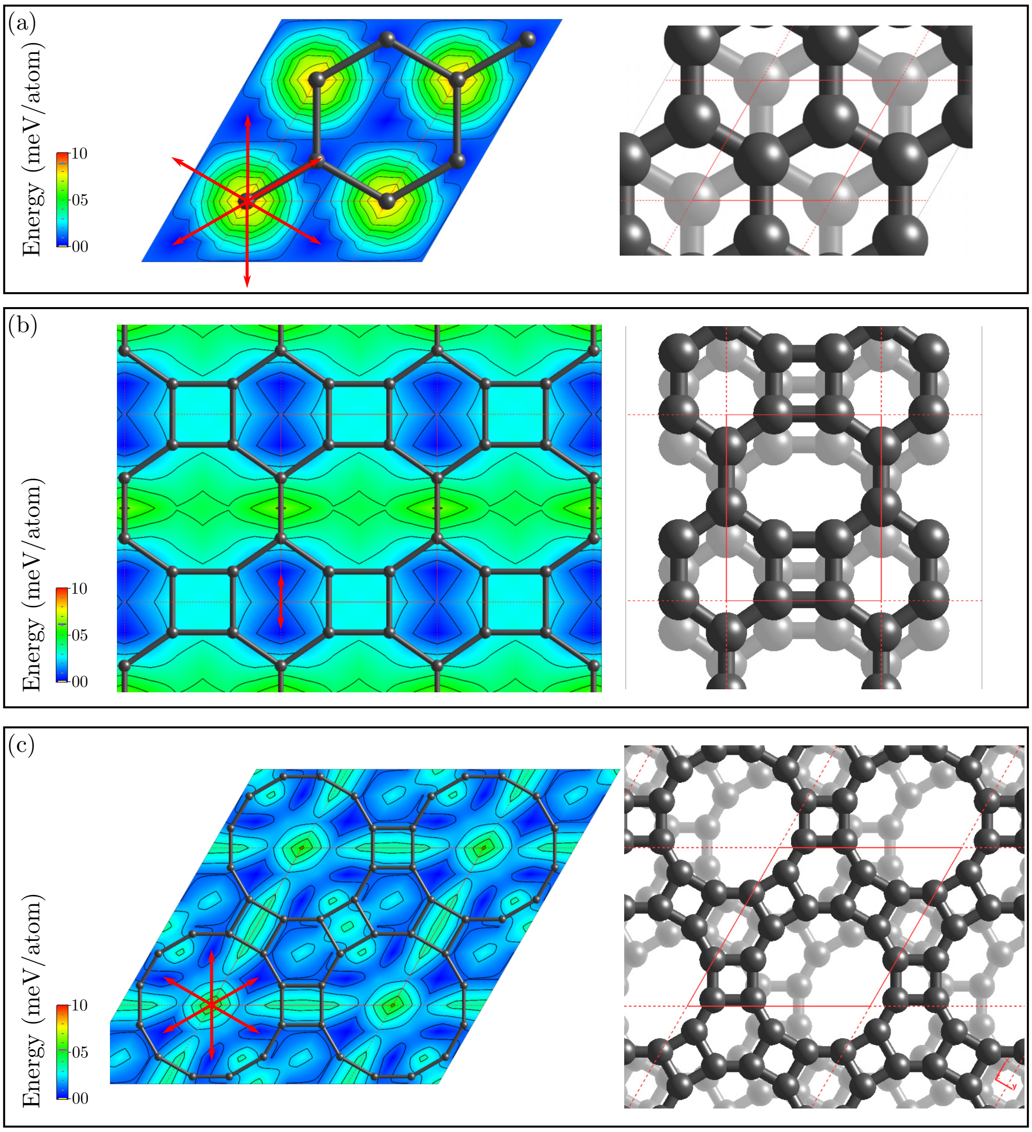

FIG. 2. Translational energy landscapes and preferential stacking of the different sp^2 carbon allotropes, including graphite (a), tetrahexaoctite (b), and tetrahexadodectite (c). The short and thick horizontal lines inside the color bars indicate the minimal and maximal value reached in a given panel. The range of the color bars ([0–10] meV/atom) is common to all panels. The red arrows indicate the translation operations to apply to one layer to go from an AA stacking to the preferential stacking visible on the right panels.

the charge transfer between atoms. The cohesive energy (E_{coh}) of the different nonlithiated carbon systems is defined as the normalized (per atom) difference between the total energy of the crystal and the energy of the isolated C atoms. Then, the lithiation energy (E_{lith}) is defined as the energy difference between the lithiated carbon material and the energies of the nonlithiated carbon material and bulk lithium normalized by the number of lithium atoms, while the stability energy (E_{stab}) is normalized with respect to the total number of atoms. Thus

$$E_{\mathrm{coh}} = \frac{E_{\mathrm{C}}^{\mathrm{bulk}} - n_{\mathrm{C}} E_{\mathrm{C}}^{\mathrm{atom}}}{n_{\mathrm{C}}}, \tag{1}$$

$$E_{\mathrm{lith}} = \frac{E_{\mathrm{C\,Li}}^{\mathrm{bulk}} - \left(n_{\mathrm{C}} E_{\mathrm{C}}^{\mathrm{bulk/atom}} + n_{\mathrm{Li}} E_{\mathrm{Li}}^{\mathrm{bulk/atom}}\right)}{n_{\mathrm{Li}}}, \tag{2}$$

$$E_{\mathrm{stab}} = \frac{E_{\mathrm{C\,Li}}^{\mathrm{bulk}} - \left(n_{\mathrm{C}} E_{\mathrm{C}}^{\mathrm{bulk/atom}} + n_{\mathrm{Li}} E_{\mathrm{Li}}^{\mathrm{bulk/atom}}\right)}{n_{\mathrm{C}} + n_{\mathrm{Li}}}, \tag{3}$$

where $E_{\mathrm{C}}^{\mathrm{bulk}}$ and $E_{\mathrm{C\,Li}}^{\mathrm{bulk}}$ are the total energies of the nonlithiated and lithiated bulk sp^2 carbon allotropes, respectively, n_{C} and n_{Li} are the number of carbon and lithium atoms in the considered bulk structure, respectively, $E_{\mathrm{C}}^{\mathrm{bulk/atom}}$ and $E_{\mathrm{Li}}^{\mathrm{bulk/atom}}$ are the total energies per atom of the nonlithiated bulk sp^2 carbon allotropes and of bulk lithium, respectively, and finally $E_{\mathrm{C}}^{\mathrm{atom}}$ is the total energy of the isolated carbon atom.

For the sake of comparison, the lithiation of graphite is also investigated with the ABINIT software [59]. In this case, the exchange-correlation energy is approximated using the GGA-PBE functional [60,61] corrected by Grimme's DFT-D2 [62], DFT-D3 [63], and DFT-D3(BJ) [64] methods, as implemented recently in the software [65]. ONCVPSP norm-conserving pseudopotentials are used [66], which include multiple projectors and describe explicitly the $1s^2 2s^1$ states of Li. A 1143 eV (42 Ha) plane-wave energy cutoff is found sufficient to guarantee the convergence of the relevant properties. Our

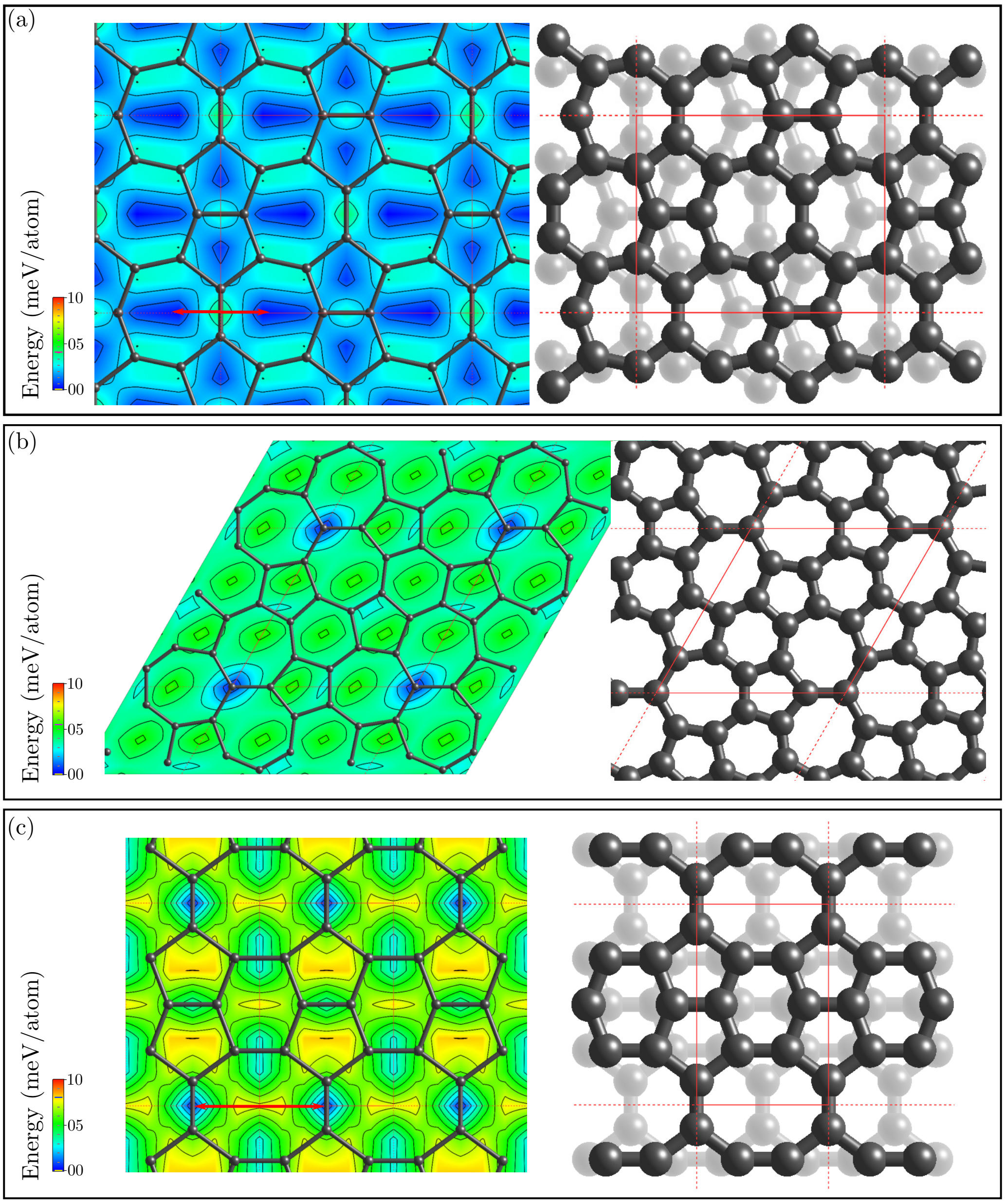

FIG. 3. Translational energy landscapes and preferential stacking of the different sp^2 carbon allotropes, including pentaheptite (a), pentahexaheptite (b), and pentahexaoctite (c). The short and thick horizontal lines inside the color bars indicate the minimal and maximal value reached in a given panel. The range of the color bars ([0–10] meV/atom) is common to all panels. The red arrows indicate the translation operations to apply to one layer to go from an AA stacking to the preferential stacking visible on the right panels.

convergence criteria for the total energy (0.5 mHa/atom) led us to use the following Monkhorst grids: $18 \times 18 \times 8$ for graphite, $4 \times 4 \times 4$ (shifted two times) for lithium, and $9 \times 9 \times 8$ for Li_1C_6. A Gaussian smearing of 0.01 Ha is used for the occupation of states.

III. GROUND STATE PROPERTIES OF THE BULK sp^2 CARBON ALLOTROPES

Before investigating the lithiation properties of the different bulk sp^2 carbon layered systems, it is important to determine their preferential stackings and their total energies ($E_{\mathrm{C}}^{\mathrm{bulk}}$) as a reference for the subsequent lithiated systems. The potential energy landscape for the stacking order of these systems is expected to be complex, with several local minima. To find the preferential stacking of the different systems illustrated in Fig. 1, the following procedure has been used. A 3D periodic unit cell containing one layer, i.e., AA stacking, is first considered and its geometry and atomic positions are optimized. Then, a 3D periodic unit cell containing two layers is constructed by doubling vertically the previous unit cell, thus still in AA stacking. Next, the top layer is rigidly shifted laterally with respect to the bottom layer inducing an AA′ stacking. A 6×6 grid of shifts is actually used to map the

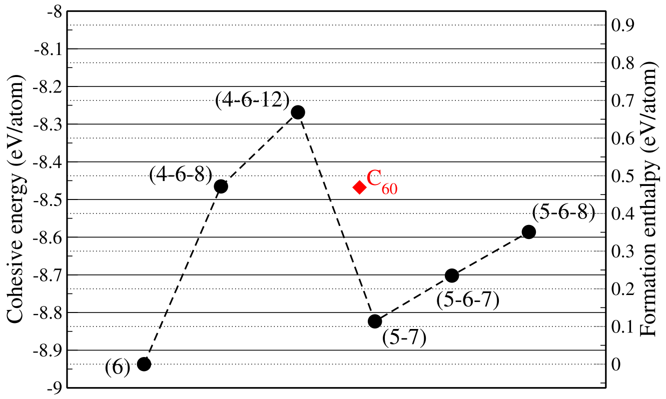

FIG. 4. Cohesive energies (E_{coh}) and formation enthalpies (E_{form}) of the six sp^2 carbon allotropes and of C_{60}. The latter was calculated separately using the SIESTA package (see main text).

TABLE I. Total energy difference per atom between, on the one hand, the alternating AA′ and rhombohedral AA′A″··· stackings and, on the other hand, the bulk AA′ stacking and the monolayer A, i.e., the stacking energy E_{stac}.

System	AA′-AA′A″··· (meV/atom)	AA′-A (meV/atom)
6	+0.225	−70.504
4-6-8	+0.036	−76.416
4-6-12	−0.277	−63.828
5-7	+0.115	−75.127
5-6-7		−76.891
5-6-8	−0.052	−77.355

different stacking configurations. For each grid point, the cell geometry and the atomic positions are frozen. Finally, the shift with the lowest energy is taken and a full optimization is performed to obtain the total energy of the preferential AA′ stacking. This lowest total energy will be used as a reference in the calculation of lithiation energies (see Secs. IV and V). The energy maps deduced from the total energy per atom on each grid point together with the fully optimized preferential stacking are displayed in Fig. 2 and Fig. 3. To further investigate the preferential stacking, rhombohedral cells are constructed from the above optimal AA′ stacking, thus corresponding to an AA′A″··· stacking and containing a single carbon layer per cell.

In the case of graphite, one recovers that the AA′ = AB stacking is favorable. It corresponds to a shift of the top layer of the order of the C-C bond length along a given C-C bond direction. The highest (layer-) sliding barrier energy is $E_{\mathrm{sb}} = 8.9$ meV per atom. It corresponds to the energy difference between AB and AA stacking configurations (for a fixed AA stacking interlayer distance of $d_{\perp} = 3.49$Å), as illustrated in Fig. 2(a). Interestingly, one can identify sliding paths which cost almost no energy ($E_{\mathrm{sb}} \lesssim 1$ meV per atom). The interlayer distance of the fully relaxed AB stacking is $d_{\perp} = 3.30$Å. The calculated graphite cohesive energy is $E_{\mathrm{coh}} = -8.937$ eV/atom. As expected, graphite is the most stable system out of the six carbon compounds investigated in this article (see Fig. 4). Finally, the AA′A″··· rhombohedral stacking, which corresponds to ABC graphite, is found to be even slightly more stable than AB graphite but by a total energy difference of only 0.225 meV/atom, hence within the energy accuracy limit of the method.

The translational energy landscapes and corresponding preferential AA′ stackings of the (4-6-8) and (4-6-12) systems are displayed in Fig. 2, and the ones of (5-6-7), (5-6-8), and (5-7) systems are displayed in Fig. 3. For the (4-6-8), the preferential stacking occurs when the second layer is slightly displaced along the y axis (armchair direction), with a shift of the order of half a C-C bond length, such that half of the atoms of the upper layer lie exactly on top of the center of a C-C bond of the bottom layer. The (4-6-12) exhibits a honeycomb lattice like in the graphene layer, but the basis consists of hexagonal carbon rings, instead of single atoms, bonded by squares. The preferential stacking occurs when half of the hexagonal carbon rings lie above square carbon rings. For the (5-7), the best stacking is predicted to occur when superposition of carbon atoms is minimal, while for the (5-6-7), it is the opposite: the best stacking is an AA stacking, i.e., where all carbon atoms of one layer are on top of the ones of the next layer. Finally, for the (5-6-8), the best stacking is obtained by avoiding the superposition of similar rings like in the (5-7) case.

For the six sp^2 carbon systems, the maximal sliding barrier energy (E_{sb}) is in a range of 5–10 meV per atom, the highest barrier being for graphite. The different cohesive energies E_{coh} are reported in Fig. 4. Graphite is obviously the most stable structure. The formation enthalpy E_{form} of the different sp^2 carbon allotropes is given by the difference between cohesive energy of graphite and their own cohesive energy ($E_{\mathrm{form}}^{\mathrm{C\ system}} = E_{\mathrm{coh}}^{\mathrm{Graphite}} - E_{\mathrm{coh}}^{\mathrm{C\ system}}$). For the sake of comparison, the formation enthalpy of C_{60} ($E_{\mathrm{form}}^{C_{60}} \sim 0.45$ eV/atom calculated separately with the SIESTA package [67] using the optB88-vdW functional [48]) is also pinpointed in Fig. 4. Most of the layered systems considered in the present study have a similar or lower formation enthalpy than C_{60}, except the (4-6-12) system.

To conclude on the preferential stacking configurations, the rhombohedral AA′A″··· stackings have been calculated and total energy differences are found to be lower than 0.3 meV/atom in all cases (see Table I). This means that one cannot clearly discriminate which are the preferential stackings between the alternating AA′ (studied above) and the rhombohedral AA′A″··· ones. For the sake of completeness, the stacking energy E_{stac} (also called the interlayer cohesive energy or exfoliation energy), defined as the total energy difference per atom between the most stable bulk AA′ phase and the monolayer phase, is calculated for each system and reported also in Table I. For graphite, the value of $|E_{\mathrm{stac}}| = 70.5$ meV per atom is in a relatively good agreement with other DFT-based calculations including various flavors of van der Waals corrections ([52–78] meV per atom) [43,68] and compared reasonably with the experimental value (52 ± 5 meV per atom) [69]. The lowest stacking energy is predicted for the 4-6-12 system (63.8 meV per atom), while the highest one is obtained for the 5-6-8 system (77.4 meV per atom).

Finally, the electronic band structures of the six sp^2 carbon systems are depicted in Fig. 5. It is easy to see that all of them are metallic systems as there is always at least one band

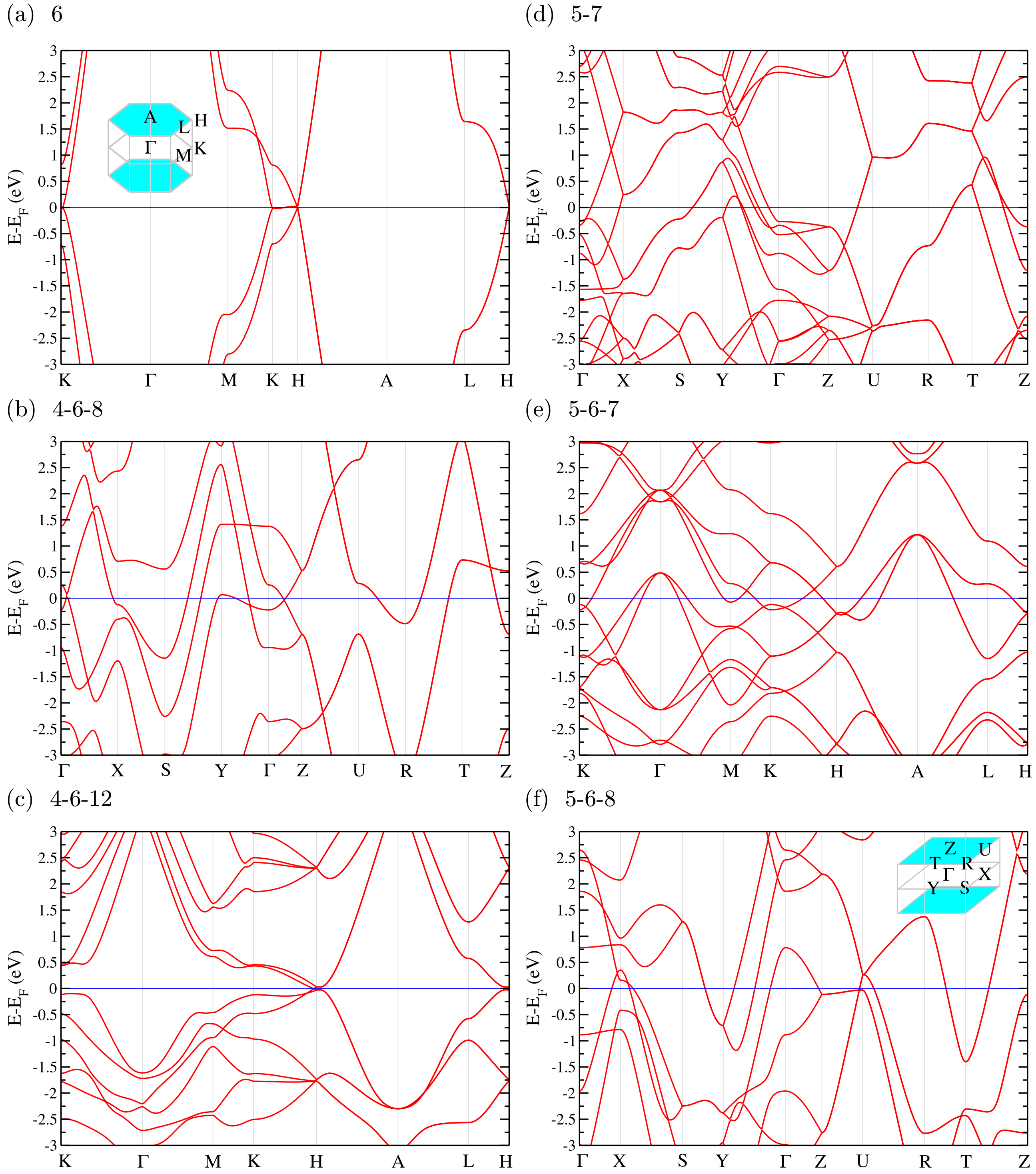

FIG. 5. Electronic band structures of the nonlithiated sp^2 carbon systems. Insets in (a) and (f) represent the two different types of Brillouin zone and their corresponding high symmetry points.

crossing the Fermi energy (E_F, aligned to zero), represented by the horizontal blue line. However, it is interesting to note that the (4-6-12) system seems to exhibit only an out-of-plane metallic character since no bands are crossing the Fermi energy for the in-plane path in the Brillouin zone, while it is the opposite behavior for the (5-7) system. Still, this requires further investigation, notably along nonhighly symmetric lines.

IV. LITHIATION IN GRAPHITE

The lithiation properties of graphite are first discussed. Such a study has been conducted several times in the past decade [16,43,70,71]; nevertheless, it is still important to reiterate it in the present context as it will serve as the reference case to compare with the rest of the sp^2 carbon

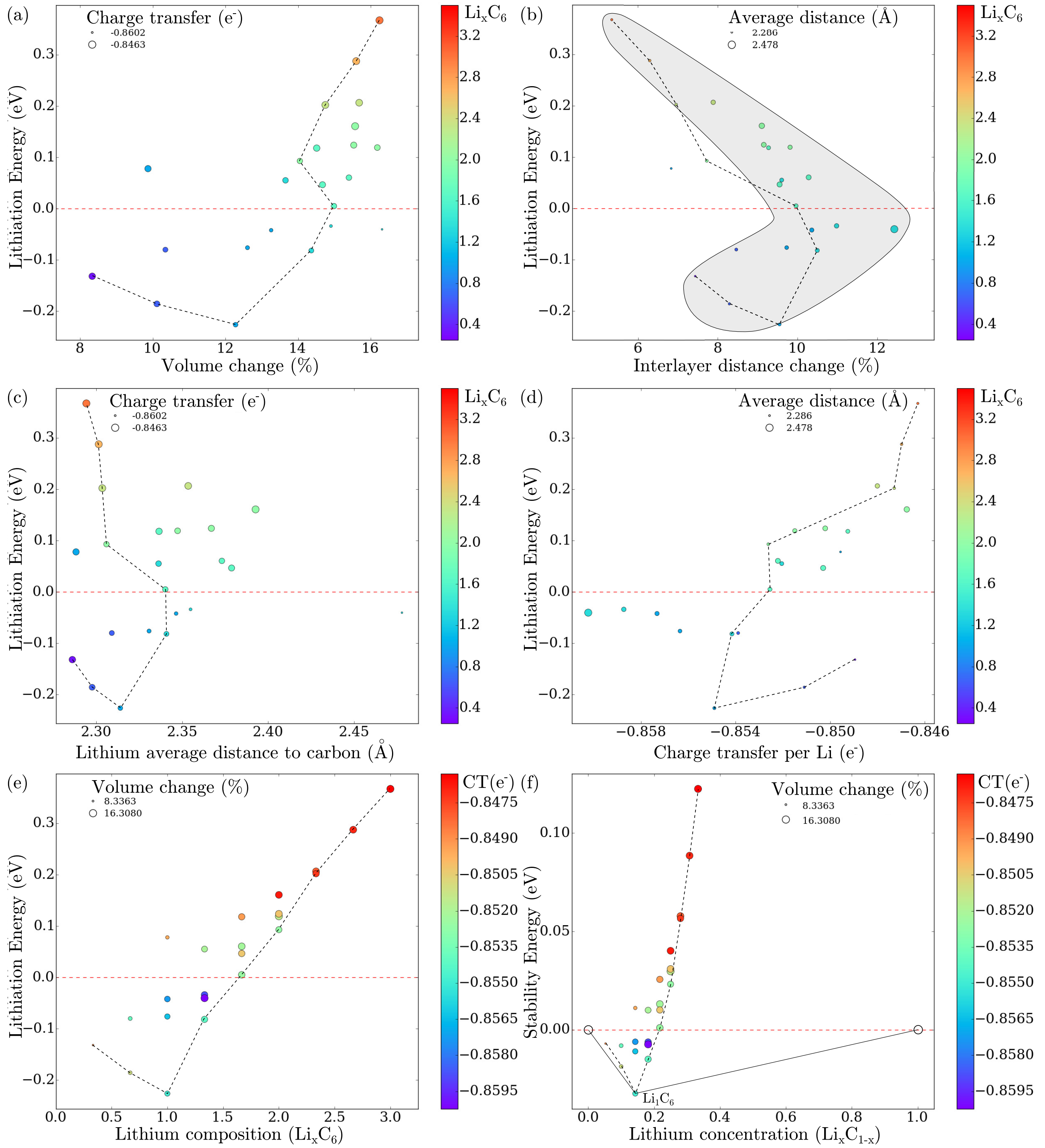

FIG. 6. Graphite (6) lithiation properties. From (a) to (e), lithiation energy as a function of volume change, interlayer distance change, Li average distance to C, CT per Li, and Li composition in Li_xC_6, respectively. Panel (f) displays stability energy as a function of Li concentration in Li_xC_{1-x}. As indicated in insets, the size of the circles straddle in between the minimal and maximal value of CT per Li (a),(c), Li average distance to C (b),(d), and volume change (e)–(f), respectively. As indicated in right-side bars, the color in the circles indicates the Li composition in Li_xC_6 (a)–(d) and the CT per Li (e),(f), respectively.

systems considered. In the previous literature, both the low and high Li concentration regimes were explored. In the low concentration regime, lithiation occurs through various *stages* (stage-n, $n > 1$), which consist in alternating empty and Li-occupied interlayer spaces. The upper-limit is stage-1, which corresponds to the intercalation of Li in between all the layers. This is also the onset of the high-concentration regime.

Since our main objective is the maximum Li storage capacity, we focus only on the high Li concentration limit, thus considering only stage-1 lithiation. The fully lithiated

TABLE II. Interlayer distance and volume of graphite unit cell ($d_{\perp}^{\text{w.o. Li}}$ and volume $^{\text{w.o. Li}}$, respectively) and of $\mathrm{Li_1C_6}$ ($d_{\perp}^{\text{w. Li}}$ and volume $^{\text{w. Li}}$, respectively), the lithiation energy (E_{lith}), and the stability energy (E_{lith}) of $\mathrm{Li_1C_6}$.

Functional/Experiment	PBE-D2	PBE-D3	PBE-D3(BJ)	optB86b-vdW	optB88 [43]	Expt.
$d_{\perp}^{\text{w.o. Li}}$ (Å)	3.22	3.48	3.38	3.30	3.36	3.34 [76]
$d_{\perp}^{\text{w. Li}}$ (Å)	3.65	3.65	3.60	3.62	3.64	3.70 [72]
Volume$^{\text{w.o. Li}}$ (Å^3)	33.8	36.7	35.5	34.8		
Volume$^{\text{w. Li}}$ (Å^3)	39.3	39.3	38.7	39.1		
E_{lith} (meV/Li atom)	−709.5	−127.9	−76.4	−226.5	−217.0	(−113.0) [43,77]
E_{stab} (meV/atom)	−101.4	−10.9	−18.3	−32.4		

phase of graphite stacks in an AA arrangement of the graphene planes. In order to investigate the lithiation of such structure, a $3 \times 3 \times 1$ supercell composed of 18 C atoms is considered. The list of potential sites to intercalate Li atoms in this structure is determined by considering the centers of hexagonal rings, i.e., in this case nine sites. All the combinations that are unique by symmetry are considered when filling the structure with up to nine Li atoms, i.e., all the possible sites. This gives 23 different lithiated structures with compositions ranging from $\mathrm{Li_{\frac{1}{3}}C_6}$ to $\mathrm{Li_3C_6}$. For all these structures, after full structural optimization, various properties are calculated such as lithiation and stability energy, average charge transfer (CT) per Li atoms, average distance between Li atoms and their first nearest-neighbor C atoms, cell volume, and interlayer distance changes with respect to the stable nonlithiated phase. All these properties are presented in Fig. 6, in different ways in order to identify possible correlations between lithiation energy and one of the above mentioned properties.

In Fig. 6(a), one observes that the maximal volume expansion with respect to AB graphite is limited to 16%. However, looking at the interlayer distance ($d_{\perp}$) variations Fig. 6(b), one notes that it increases up to ∼12% when approaching the lithiation energy limit ($E_{\text{lith}} = 0$ eV), before decreasing when incorporating more Li than graphite can stabilize. This behavior is represented by the transparent gray area exhibiting a *boomerang* shape. The latter is simply a rough guide for the eyes. In the very high Li concentration regime ($E_{\text{lith}} > 0$ eV), the in-plane lattice increases monotonically and compensates the relative interlayer distance decrease in order to obtain a volume increase that saturates around 16%. The average distance between Li atoms and their first nearest carbon neighbors typically ranges between 2.30 and 2.40 Å, displaying an important dispersion [Fig. 6(c)]. The average CT per Li atom is less negative (i.e., each atom gives less electrons) as the lithiation energy increases [Fig. 6(d)]. Above the lithiation energy limit, a quasilinear dependence on the CT can be distinguished, indicating a correlation between lithiation energy and CT. The threshold CT value separating positive from negative lithiation energies is $-0.852|e|$. The lithiation energy E_{lith} as a function of Li concentration is plotted in Fig. 6(e), where the dashed line connects all minimum E_{lith} for a given concentration. This dashed line, representing hence the minimal lithiation energy path, is also reported in all panels. The maximal concentration that has a negative lithiation energy is $\mathrm{Li_{\frac{4}{3}}C_6}$ with energy $E_{\text{lith}} = -0.09$ eV. This concentration is slightly higher than the known value of $\mathrm{Li_1C_6}$, which we also found at $E_{\text{lith}} \sim -0.23$ eV. Despite the fact that its lithiation energy is negative, this $\mathrm{Li_{\frac{4}{3}}C_6}$ phase is not observed experimentally. This is because this phase does not lie on the convex hull of the phase diagram as calculated in Fig. 6(f). Although $\mathrm{Li_{\frac{4}{3}}C_6}$ is energetically favorable when compared to bulk graphite and bulk lithium phases, it is less favorable than $\mathrm{Li_1C_6}$ plus bulk lithium phase. This means that the $\mathrm{Li_{\frac{4}{3}}C_6}$ phase would decompose into $\mathrm{Li_1C_6}$ and bulk lithium, i.e., lithium plating would occur. This analysis is of importance because finding the maximum lithiation requires one to consider not only the sign of the lithiation energy but also the position on the convex hull of the stability phase diagram. The in-plane lattice constant and interlayer distance of the most stable $\mathrm{Li_1C_6}$ phase are 2.50 Å and 3.62 Å, respectively, and leads to a 12.3% volume expansion, which is in agreement with previous results in the literature [43,72]. Going back to Figs. 6(a)–6(d), and following now the dashed line, one observes even more clearly a rapid increase of volume expansion followed by a much slower increase as E_{lith} becomes positive which is explained by the relative decreasing interlayer distance in this regime. Considering only the dashed line in panel (c), one notes that the average Li-C distance is actually less dispersed and is centered on 2.30 Å. If one discards the four points with negative E_{lith} on the left part of panel (d), i.e., not lying on the minimal lithiation energy path represented by the dashed line, our first guess that lithiation energy is correlated to charge transfer is confirmed.

For pristine (AB) graphite and the most stable $\mathrm{Li_1C_6}$ phase, first-principles calculations were also conducted with the ABINIT software using different functionals. The energy and the structural parameters obtained with the different approaches are compared with experimental data in Table II. In this table, the volume of $\mathrm{Li_1C_6}$ phase is normalized to the (AB) graphite unit cell in order to appreciate the volume expansion. We also compare our results with previous DFT calculations [43] relying on the optB88 exchange-correlation functional, and with experimental data. Note that, for the lithiation energy E_{lith} (and the stability energy E_{stab}), a rather large variation is observed among the different functionals used. We suspect that such big discrepancies are related to the proper description of the long range electron-electron correlations in metals [73]. More specifically, the difference in cohesion energy of graphite and lithium as discussed in [65] and [74,75], respectively, does not explain such discrepancies. The issue is thus related to the

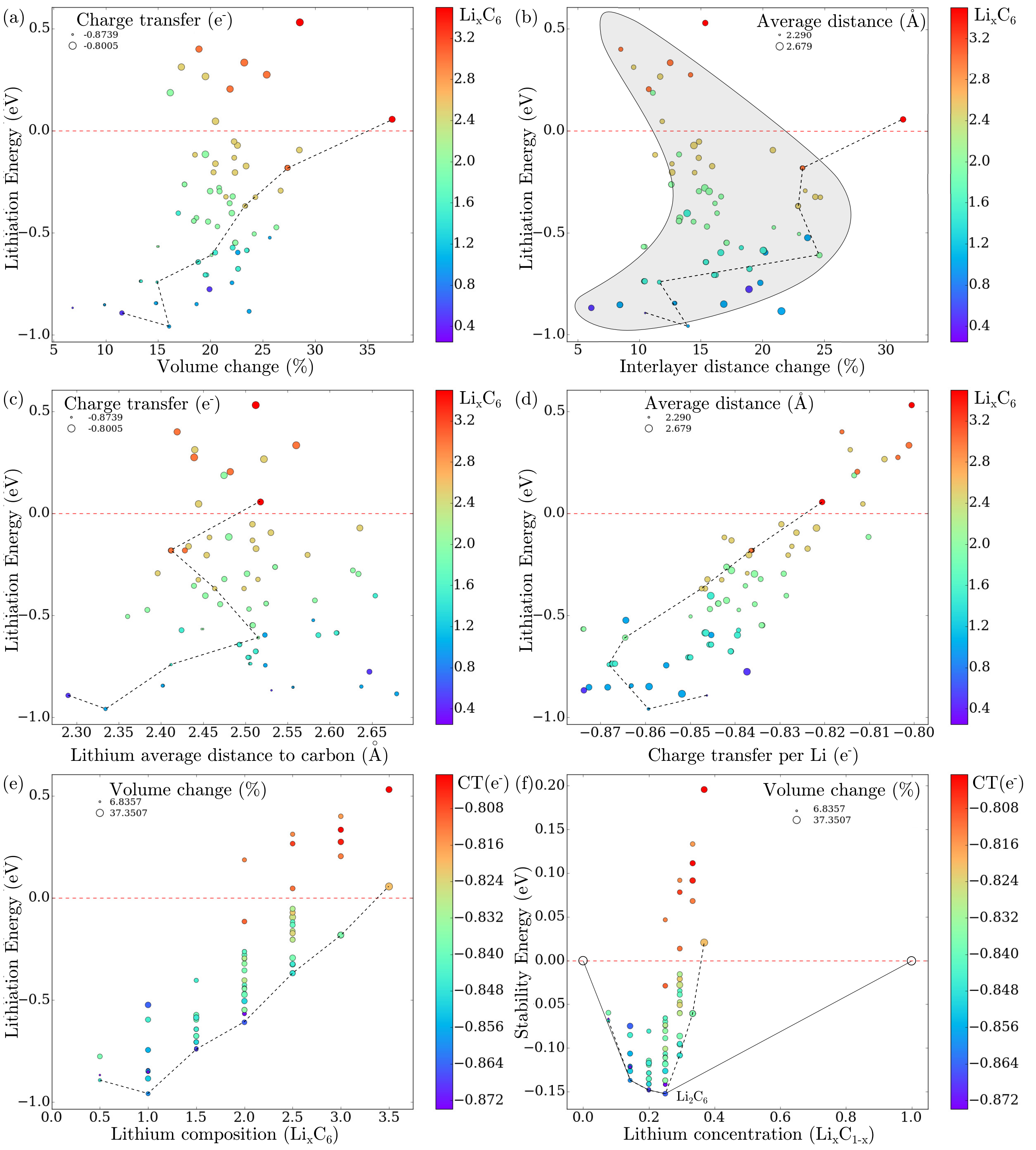

FIG. 7. Tetrahexaoctite (4-6-8) lithiation properties. From (a) to (e), lithiation energy as a function of volume change, interlayer distance change, Li average distance to C, CT per Li, and Li composition in Li_xC_6, respectively. Panel (f) displays stability energy as a function of Li concentration in Li_xC_{1-x}. As indicated in insets, the size of the circles straddle in between the minimal and maximal value of CT per Li (a),(c), Li average distance to C (b),(d), and volume change (e),(f), respectively. As indicated in right-side bars, the color in the circles indicates the Li composition in Li_xC_6 (a)–(d) and the CT per Li (e),(f), respectively.

proper description of Li_1C_6 but is beyond the scope of the paper. However, these errors are expected to be systematic for all the systems studied here and, therefore, the trends and comparisons are still valid. Finally, the experimental value of E_{lith} appearing in Table II cannot be compared directly to the calculated values as it comes from room temperature measurements, while calculations are performed at 0 K.

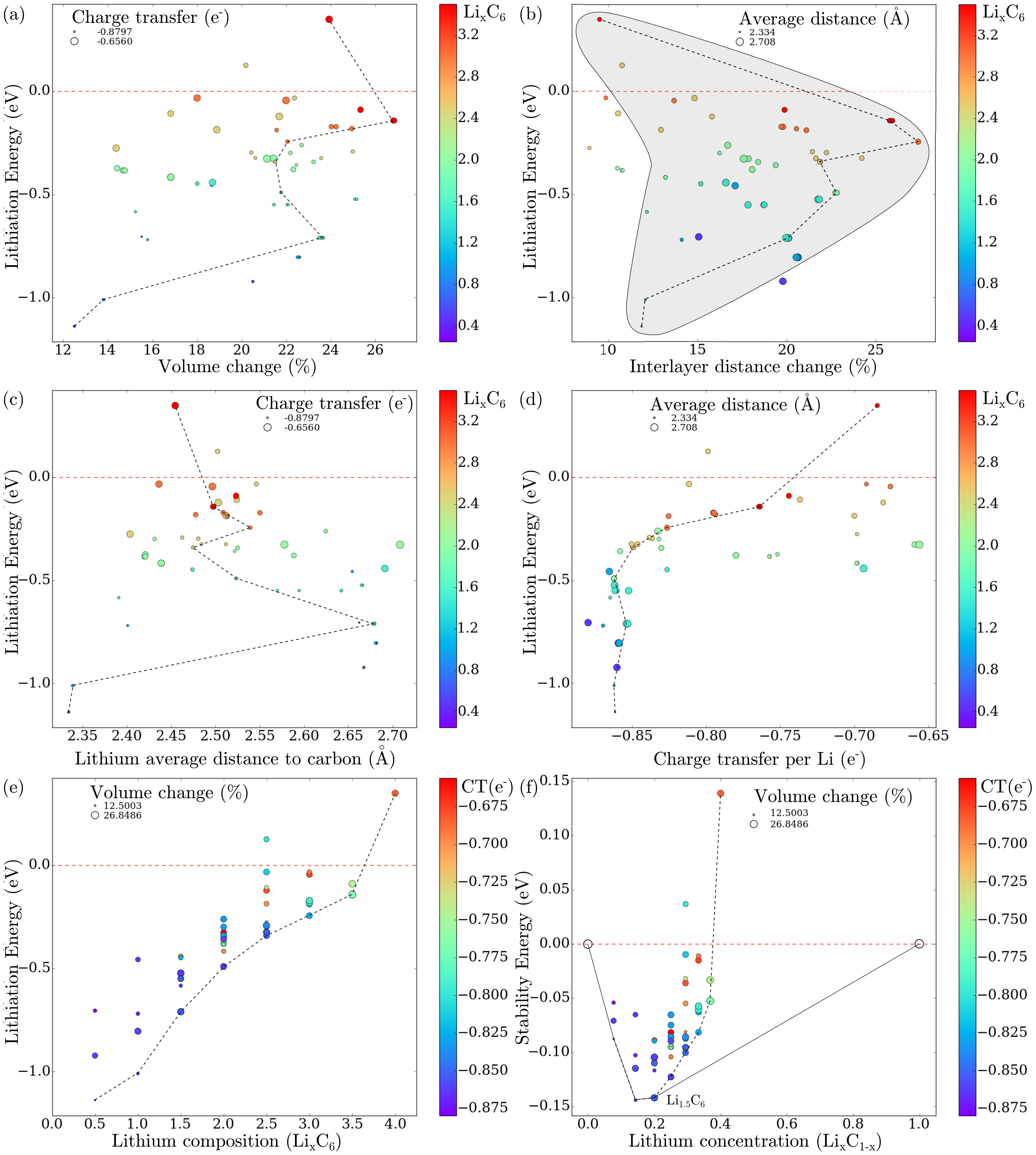

FIG. 8. Tetrahexadodectite (4-6-12) lithiation properties. From (a) to (e), lithiation energy as a function of volume change, interlayer distance change, Li average distance to C, CT per Li, and Li composition in $\mathrm{Li}_x\mathrm{C}_6$, respectively. Panel (f) displays stability energy as a function of Li concentration in $\mathrm{Li}_x\mathrm{C}_{1-x}$. As indicated in insets, the size of the circles straddle in between the minimal and maximal value of CT per Li (a),(c), Li average distance to C (b),(d), and volume change (e),(f), respectively. As indicated in right-side bars, the color in the circles indicates the Li composition in $\mathrm{Li}_x\mathrm{C}_6$ (a)–(d) and the CT per Li (e),(f), respectively.

V. LITHIATION IN sp^2 CARBON ALLOTROPES

In the present section, the lithiation of the different bulk sp^2 carbon allotropes will be presented. First, the lithiation properties of the tetrahexaoctite (4-6-8) are discussed. As for graphite, the focus is on the high lithiation limit and only the AA stacking is considered as a starting point because of computational limitations. However, one notes that the cell geometry is free to relax and thus the c axis can end up in a nonorthogonal configuration with respect to the basal plane, which would then induce a final stacking different from AA.

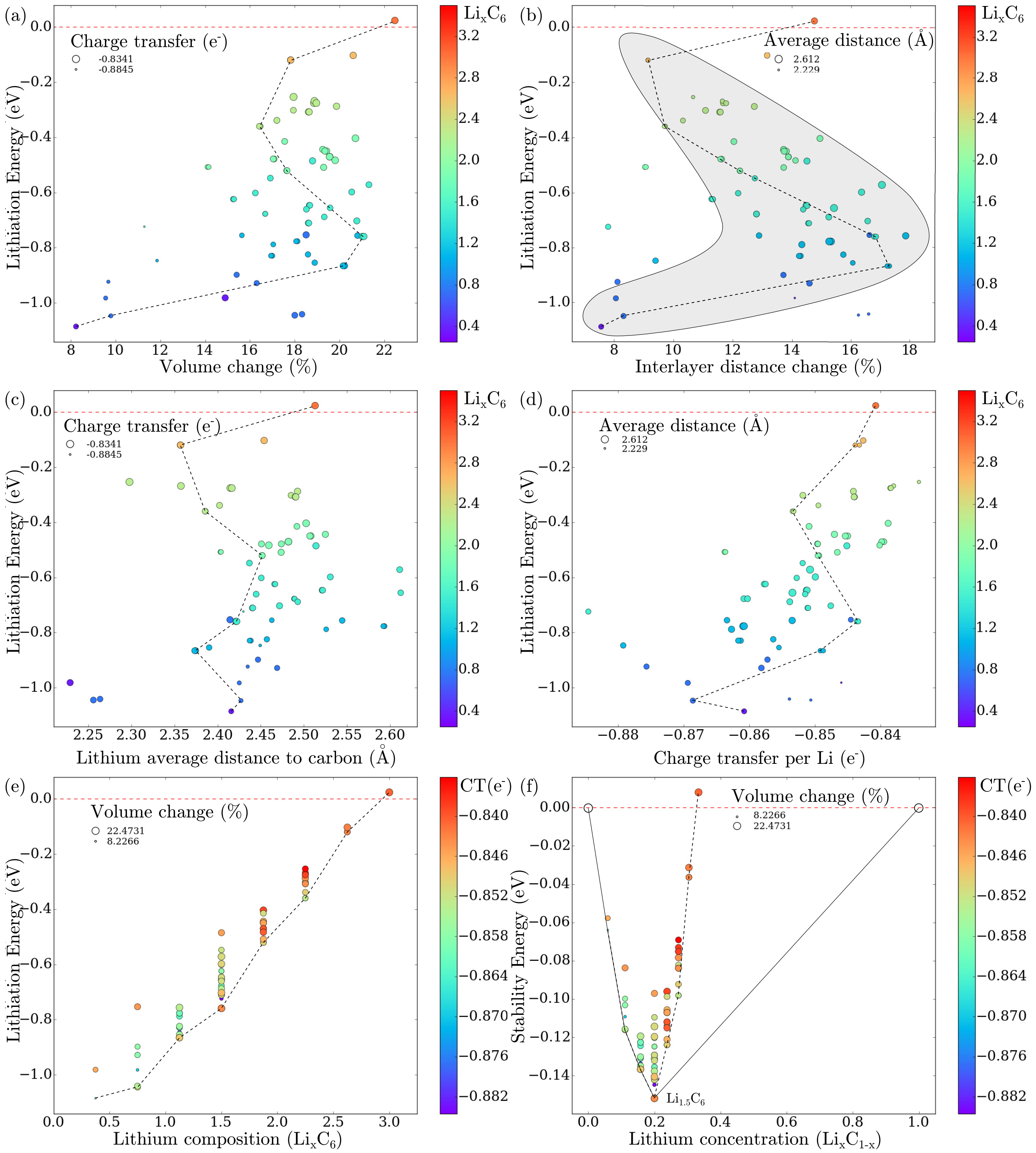

FIG. 9. Pentaheptite (5-7) lithiation properties. From (a) to (e), lithiation energy as a function of volume change, interlayer distance change, Li average distance to C, CT per Li, and Li composition in Li_xC_6, respectively. Panel (f) displays stability energy as a function of Li concentration in Li_xC_{1-x}. As indicated in insets, the size of the circles straddle in between the minimal and maximal value of CT per Li (a),(c), Li average distance to C (b),(d), and volume change (e),(f), respectively. As indicated in right-side bars, the color in the circles indicates the Li composition in Li_xC_6 (a)–(d) and the CT per Li (e),(f), respectively.

The reference bulk energy ($E_C^{\text{bulk/atom}}$) used in the lithiation energy calculation is still the one obtained for the preferential stacking of the nonlithiated structure (as done for graphite). In order to investigate the possible arrangement of lithium in the (4-6-8) structure, a 2 × 1 × 1 supercell is constructed. In total, 83 nonequivalent starting configurations for positioning the Li atoms are found. The different properties (interlayer distance, volume expansion, charge transfer, lithium average distance to carbon, and lithiation and stability energies) are presented in Fig. 7. The results are first analyzed ignoring for

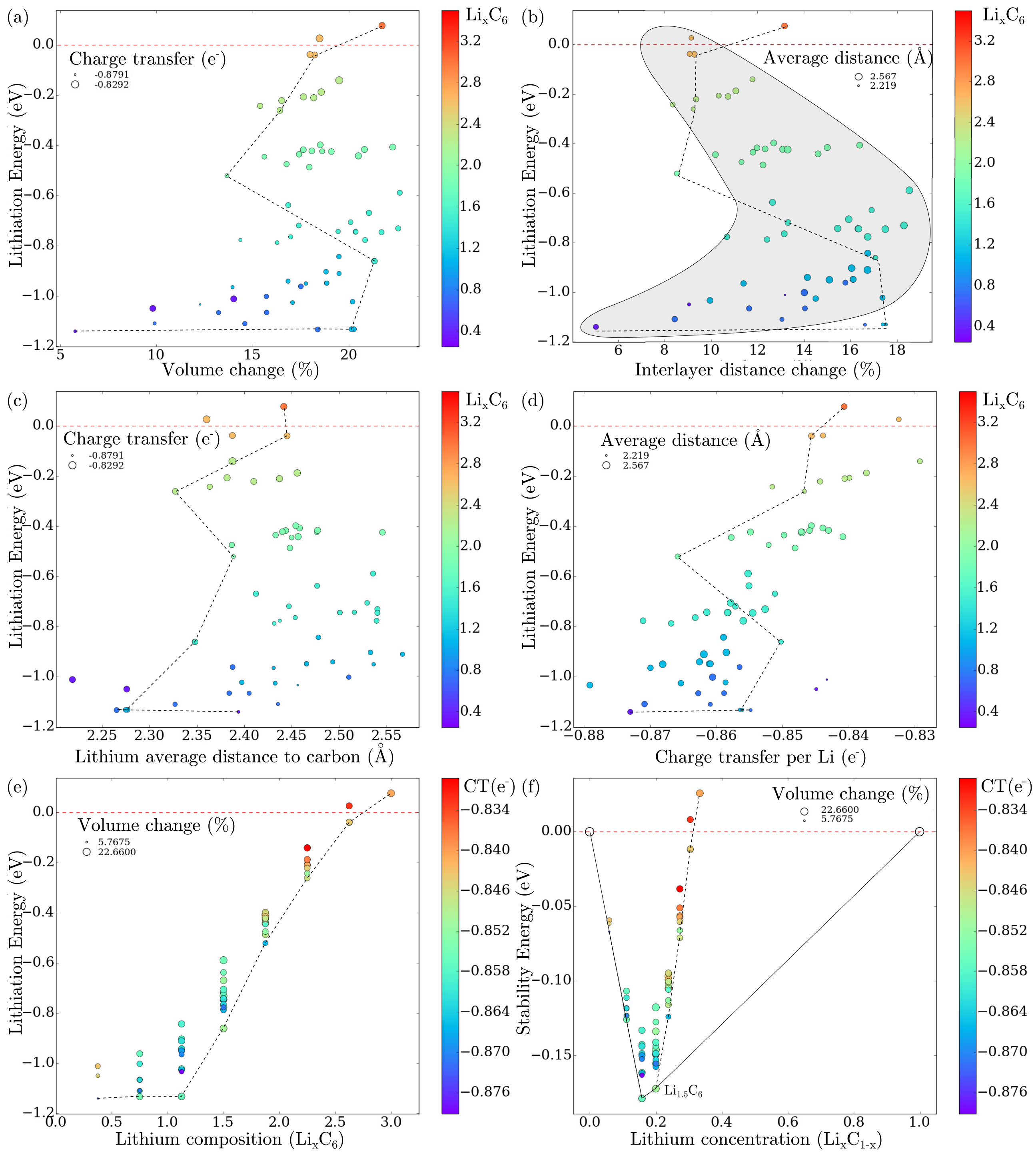

FIG. 10. Pentahexaheptite (5-6-7) lithiation properties. From (a) to (e), lithiation energy as a function of volume change, interlayer distance change, Li average distance to C, CT per Li, and Li composition in $\mathrm{Li}_x\mathrm{C}_6$, respectively. Panel (f) displays stability energy as a function of Li concentration in $\mathrm{Li}_x\mathrm{C}_{1-x}$. As indicated in insets, the size of the circles straddle in between the minimal and maximal value of CT per Li (a),(c), Li average distance to C (b),(d), and volume change (e),(f), respectively. As indicated in right-side bars, the color in the circles indicates the Li composition in $\mathrm{Li}_x\mathrm{C}_6$ (a)–(d) and the CT per Li (e),(f), respectively.

the moment the dashed line representing the minimal lithiation energy path. The maximal volume increase is higher than in graphite by a factor of two–three, that is a volume change up to ∼37% at most, but most of the values are centered on 20% [Fig. 7(a)]. The interlayer distance changes from 5% to 31% and its variation roughly displays a *boomerang* shape, as for graphite although a bit more scattered, where the cusp is now located at $E_{\mathrm{lith}} = -0.3$ eV instead of $E_{\mathrm{lith}} = 0$ eV [Fig. 7(b)]. The range of average distances between Li atoms and their first nearest carbon neighbors is wider than in graphite

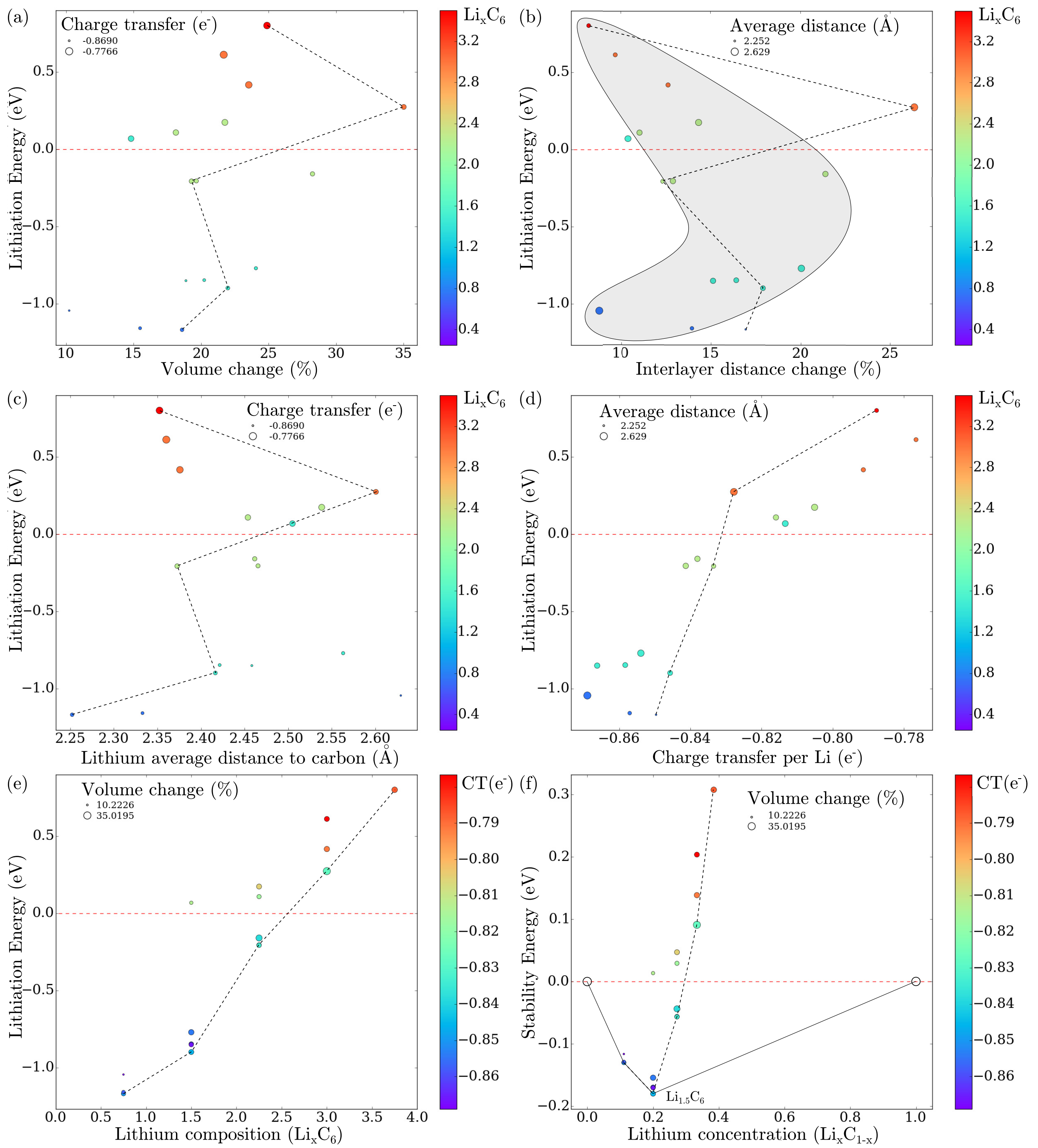

FIG. 11. Pentahexaoctite (5-6-8) lithiation properties. From (a) to (e), lithiation energy as a function of volume change, interlayer distance change, Li average distance to C, CT per Li, and Li composition in Li_xC_6, respectively. Panel (f) displays stability energy as a function of Li concentration in Li_xC_{1-x}. As indicated in insets, the size of the circles straddle in between the minimal and maximal value of CT per Li (a),(c), Li average distance to C (b),(d), and volume change (e),(f), respectively. As indicated in right-side bars, the color in the circles indicates the Li composition in Li_xC_6 (a)–(d) and the CT per Li (e),(f), respectively.

(here from 2.30 to 2.65 Å) but exhibits also rather dispersed results [Fig. 7(c)]. The average CT per Li atom seems to display a quasilinear dependence with the lithiation energy over the entire set of points [Fig. 7(d)]. This supports the similar behavior discussed above for graphite. The threshold CT value for the tetrahexaoctite is lowered to $-0.820|e|$. The lithiation energy curve as a function of Li concentration suggests that stable lithiation can be obtained up to Li_3C_6 [Fig. 7(e)]. However, by plotting the convex hull of the stability phase diagram [Fig. 7(f)], the highest stable lithium concentration is

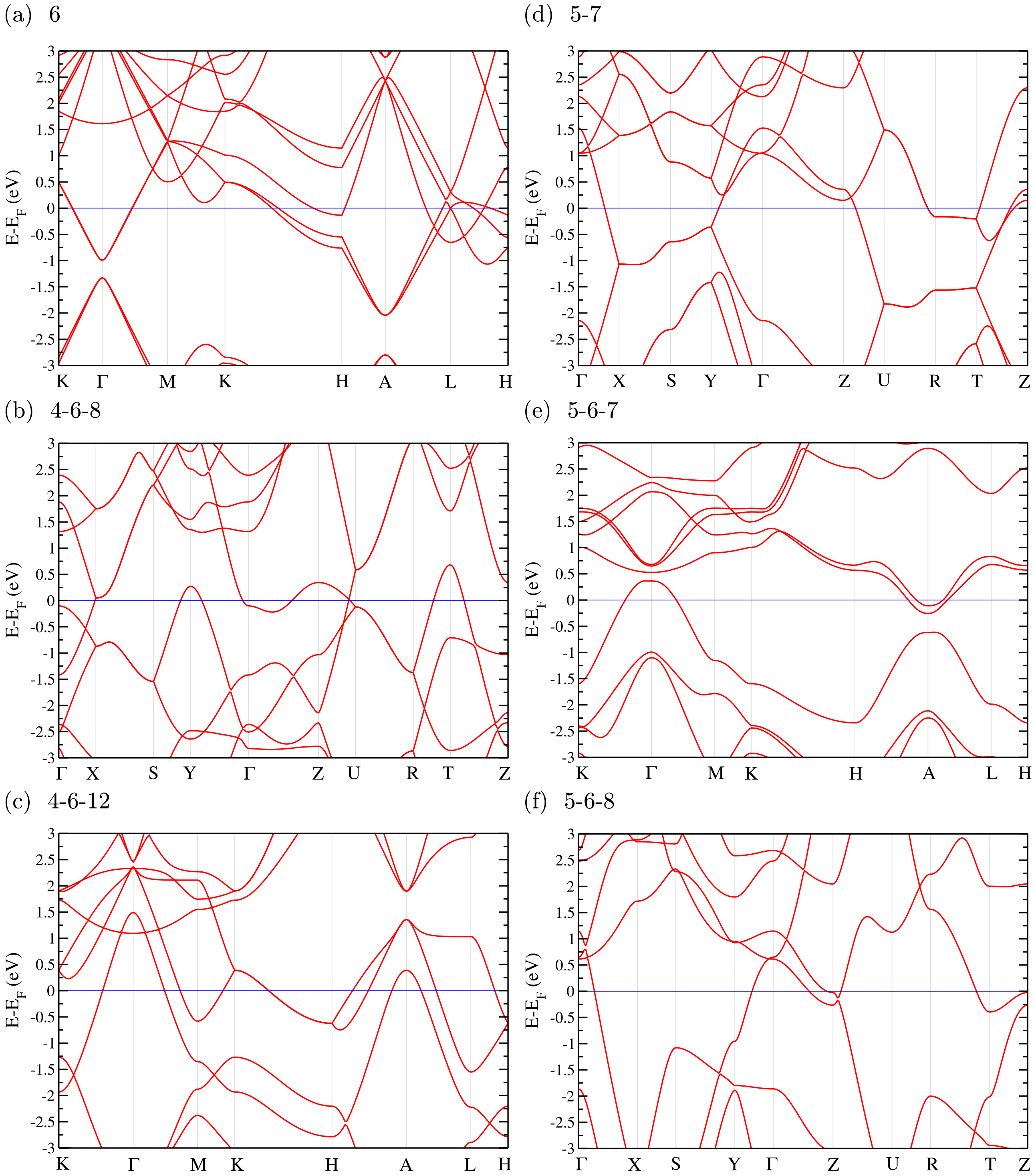

FIG. 12. Electronic band structures of the lithiated sp^2 carbon systems.

identified as Li_2C_6, i.e., 744.5 mAh/g, which is twice higher than the known graphite specific capacity (Li_1C_6) [78]. The lithiation energy associated with this Li_2C_6 phase is −0.61 eV and its interlayer distance is 4.01 Å. Moreover, for this phase, the *c* axis is no longer perpendicular to the basal plane, meaning that the stacking of this lithiated phase is not AA. Indeed, as seen in Fig. 13 gathering all the stable lithiated structures, the *c* axis of the 4-6-8 rectangular 2 × 1 × 1 supercell is indeed tilted along the *x* axis, the one along which the hexagons connect to the squares which is also globally the easiest sliding direction according to Fig. 2. Finally, this phase is accompanied by a slight buckling of the basal plane of 0.27 Å. Looking at the minimal lithiation energy path represented by the dashed line in all panels, one notes that, different from graphite, in the very high lithium concentration regime, the interlayer distance continues to increase up to 31% instead of following the second part of the *boomerang*. However, only two configurations are sampling this very high concentration; thus larger supercells

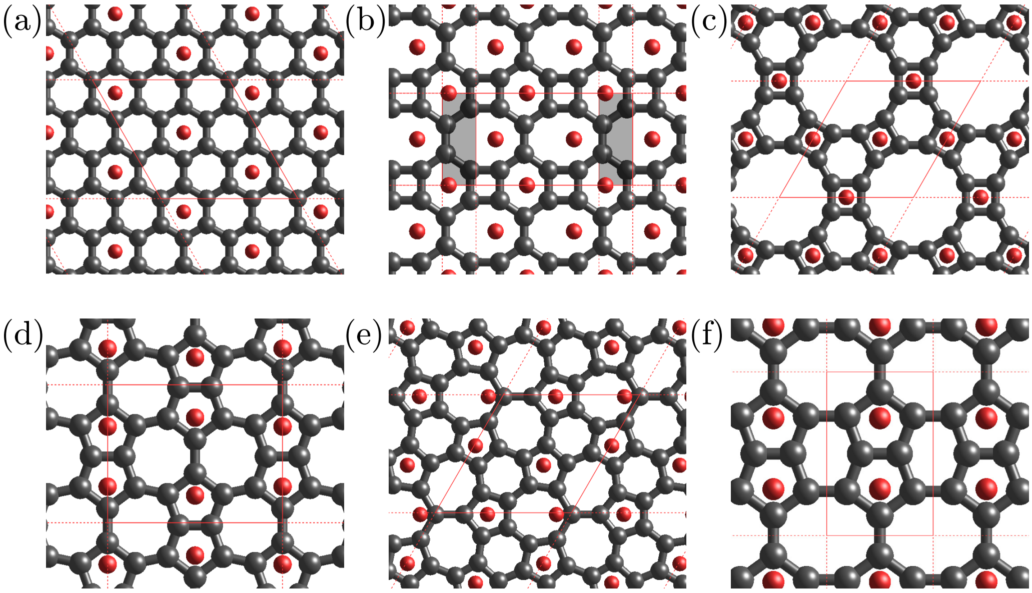

FIG. 13. Relaxed geometries of the different most lithiated and stable sp^2 carbon allotropes considered. From (a) to (f): graphite (6), tetrahexaoctite (4-6-8), tetrahexadodectite (4-6-12), pentaheptite (5-7), pentahexaheptite (5-6-7), and pentahexaoctite (5-6-8), respectively. The shadowy part in (b) shows that the c axis is tilted and thus no more orthogonal to the basal plane.

might be required to investigate more of them. The average Li-C distance is now limited to 2.52 Å and a linear behavior between lithiation energy and charge transfer is confirmed with kind of a *hook* at the onset, as for graphite, which corresponds to the initial decrease of lithiation energy at low lithium concentration.

The lithiation properties of the tetrahexadodectite (4-6-12), the pentaheptite (5-7), the pentahexaheptite (5-6-7), and the pentahexaoctite (5-6-8) are presented in Figs. 8, 9, 10, and 11, respectively. In these four other systems, the maximal volume increases are in a 20–30% range, while their average values are between 15 and 20%. The interlayer distance variations still display a *boomerang* shape. However, following the dashed line an *S*, or zigzag, shape is observed for 5-7 and 5-6-7 with the last point going out the *boomerang* in the very high Li concentration regime. Again this might be related to an insufficient configuration sampling. Except for the 4-6-12 for which the trend is more complex, a quasilinear increase in the lithiation energy is also induced by the decrease of the charge transfer per Li atom. One also observes that the dashed line, i.e., minimal lithiation energy path, can oscillate around this linear relationship. In the case of 4-6-12, the charge transfer is rather constant ($\sim -0.86|e|$) at the onset of lithiation, and then only seem to follow the linear trend. A charge transfer threshold value of $\sim -0.84|e|$ is identified in order to obtain negative lithiation energies, except again for the 4-6-12 case for which the lithiation energy is maintained to negative values up to charge transfer value as small as $\sim -0.71|e|$. The range of average Li-C distance is 2.20–2.70 Å among all the considered systems but no clear cross dependencies were evidenced. Following the negative lithiation energy as maximum lithiation criterion, one would obtain a Li capacity of $Li_{2.5}C_6$ for the 5-6-8 system and up to $Li_{3.5}C_6$ for the 4-6-12 system. However, as mentioned above, it is important to calculate the stability energy and identify the convex hull curve to determine the most lithiated and stable phase which in all the four cases is actually $Li_{1.5}C_6$.

Finally, the band structures and the atomic structures of the most lithiated and stable phases of the six considered sp^2 carbon systems are displayed in Figs. 12 and 13, respectively. All of them remain metallic upon lithiation, with analogous band dispersion characters which should lead to interesting electronic conductive properties. Interestingly, one notices in Fig. 13 that Li atoms reside preferentially on small carbon rings, i.e., squares, pentagons, and hexagons rather than on heptagons, octagons, or dodecagons, although Li atoms can go to these large carbon rings when favored by a minimized steric hindrance.

Table III summarizes the most significant information, which allows us to compare the most lithiated and stable phases of the different sp^2 carbon layered systems. It is rather obvious that the most interesting candidate is the tetrahexaoctite (4-6-8) system. It exhibits the highest gravimetric and volumetric capacities, larger than in graphite by a factor 2. Moreover, this specific system presents the highest probability to be experimentally synthesized using the bottom-up chemistry approach based on biphenylene monomers as discussed earlier [33]. While it is associated with a rather large interlayer distance increase of 0.792 Å, i.e., +24.58%, the total volume increase remains limited to 20.10%. The basal plane axes are slightly contracted as a probable consequence of the slight layer buckling. Although the volume expansion is larger than that of graphite by a factor 1.6, it sounds still acceptable as this deformation may still be endured by the material and may thus preserve a good cyclability (although this assessment necessitates further investigation). Although we have seen that the threshold CT value for positive lithiation energy was decreasing from $-0.85|e|$ in graphite to $-0.82|e|$ in tetrahexaoctite and even to $-0.71|e|$ in tetrahexadodectite, the CT value at the most lithiated and stable phase stays relatively

TABLE III. Number of nonequivalent starting configurations for lithiation studies of the different sp^2 carbon allotropes considered, the interlayer distance in the stable nonlithiated ($d_\perp^{\text{w.o. Li}}$) structure, and then for the most lithiated and stable phase ($d_\perp^{\text{w. Li}}$), the lithiation energy (E_{lith}), the stability energy (E_{stab}), the gravimetric and volumetric capacities, volume expansion, average charge transfer, and Li-C distance.

sp^2 carbon allotrope	(6)	(4-6-8)	(4-6-12)	(5-7)	(5-6-7)	(5-6-8)
nb of starting noneq. config.	23	83	64	72	63	17
Grav. cap. (mAh/g)	372.2	744.5	558.4	558.4	558.4	558.4
Vol. cap. (mAh/cm^3)	833.2	1617.4	955.1	1180.8	1187.8	1171.0
$d_\perp^{\text{w.o. Li}}$ (Å)	3.302	3.221	3.273	3.259	3.255	3.229
$d_\perp^{\text{w. Li}}$ (Å)	3.617	4.013	3.930	3.807	3.810	3.808
Vol. exp. (%)	12.28	20.10	23.62	21.09	21.35	21.98
Avg. CT (|e|)	−0.855	−0.864	−0.854	−0.843	−0.850	−0.846
Avg. Li-C dist. (Å)	2.31	2.52	2.68	2.42	2.35	2.42
E_{lith} (eV/Li atom)	−0.227	−0.609	−0.710	−0.759	−0.861	−0.899
E_{stab} (eV/atom)	−0.032	−0.152	−0.142	−0.152	−0.172	−0.180

constant among the different systems, i.e., around $-0.85|e|$. In the new sp^2 carbon layered systems, the average Li-C distance is globally larger than in graphite, in accordance with the larger volume increase. The tetrahexaoctite (4-6-8) also displays the most modest increase in lithiation energy (E_{lith}) compared to graphite. This may be useful as one should keep the battery voltage difference to reasonable values. It is finally also interesting to note that the five new sp^2 carbon systems demonstrate higher stability of the lithiated phase, as E_{stab} becomes at least 100 meV/atom more negative.

VI. CONCLUSION

The ground state properties of various 3D bulk sp^2 carbon structures with various stackings [namely graphite (6), tetrahexaoctite (4-6-8), tetrahexadodectite (4-6-12), pentahexaheptite (5-6-7), pentahexaoctite (5-6-8), and pentaheptite (5-7)] have been calculated using first-principles simulations. In particular, the structural and electronic properties have been discussed, including the stacking configurations and interlayer distances. Then, the lithiation properties of these six sp^2 carbon structures have been investigated, focusing on the upper limit of lithium insertion, i.e., theoretical lithium capacity, an important parameter for modern batteries. For graphite, the reference case, a lithium composition of Li_1C_6 for a volume expansion of ∼12% was obtained in good agreement with existing literature. For the other systems, a maximum lithium capacity of $Li_{1.5}C_6$ was found with the exception of the tetrahexaoctite (4-6-8) structure which exhibits the highest capacity of Li_2C_6 at the cost of a relatively moderate volume expansion of ∼20%. The systematic study of the lithiation of these sp^2 carbon structures shows a linear dependence between lithiation energy and charge transfer between Li atoms and carbon host, which is hence a key parameter for enhancing the lithium capacity. The essential difference between graphite and the five other systems is that the lithiation energy remains negative up to lower charge transfer values, as if the referential for the zero lithiation energy would have been shifted in structures containing nonhexagonal carbon rings. The Li atoms are globally placed favorably on the low carbon membered rings, such as squares and pentagons, with an exception for the tetrahexaoctite (4-6-8) where steric hindrance seems to overcome this rule of thumb.

In our study, we have considered the stability energy with the corresponding convex hull energy curve demonstrating that the lithiation energy is not sufficient to conclude on the true maximal lithium capacity. However, the dynamics of lithiation have not been investigated. It requires the determination of Li diffusion barriers and the identification of optimal diffusion path and other associated more complex diffusion phenomena [79–81]. At last, the validity of the present results are limited to low temperatures and high lithium concentration. It has been shown for instance that phonons play an important role for intermediate graphite lithiation stages [43]. Finally, another important issue of the anode in Li-ion batteries is the formation of a solid-electrolyte interface (SEI) [82]. These aspects are beyond the scope of the present article. However, the importance of finite temperature, dynamics, and the impact of SEI formation should be addressed to determine the best candidates. Nevertheless, it is expected, for the case of SEI formation, to be relatively small, similar to the case of graphite [83]. Besides Li-ion batteries, sodium (Na)-ion ones are currently investigated more and more because of the greater earth abundance of sodium compared to lithium. For graphite, it is well known that the Na intercalation is greatly limited. This is believed to be due to a too small interlayer distance which can be overcome using expanded graphite [84], where interlayer distance $d_\perp^{\text{w.o. Li}} = 4.3$ Å. In view of the calculated interlayer distances for the present sp^2 carbon allotropes, it seems fair to assume that it will not work either. However, a recent study tends to demonstrate that Na is actually a particular case among all other alkali-metal elements [85].

ACKNOWLEDGMENTS

The authors acknowledge financial support from the BATWAL project sponsored by the Région Wallone (No. 1318146), from the Fédération Wallonie-Bruxelles through the Action de Recherche Concertee (ARC) on 3D nanoarchitecturing of 2D crystals (No. 16/21-077), and the BATTAB project (No. 14/19-057), from the European Union's Horizon 2020 researchers and innovation programme (No. 696656), from the Marcel De Merre Prize (UCL), from the Fonds de la Recherche Scientifique de Belgique (F.R.S.-FNRS) under the PDR project (No. T.00014.13), and through a FRIA grant (B.V.T.). Computational resources have been provided by the supercomputing facilities of the Université catholique de Louvain (CISM/UCL) and the Consortium des Équipements de Calcul Intensif en Fédération Wallonie Bruxelles (CÉCI) funded by the Fond de la Recherche Scientifique de Belgique (F.R.S.-FNRS) under convention No. 2.5020.11.

[1] S. Flandrois and B. Simon, Carbon materials for lithium-ion rechargeable batteries, Carbon **37**, 165 (1999).
[2] M. Mohri, N. Yanagisawa, Y. Tajima, H. Tanaka, T. Mitate, S. Nakajima, M. Yoshida, Y. Yoshimoto, T. Suzuki, and H. Wada, Rechargeable lithium battery based on pyrolytic carbon as a negative electrode, J. Power Sources **26**, 545 (1989).
[3] J.-M. Tarascon and M. Armand, Issues and challenges facing rechargeable lithium batteries, Nature (London) **414**, 359 (2001).
[4] M. N. Obrovac and L. J. Krause, Reversible cycling of crystalline silicon powder, J. Electrochem. Soc. **154**, A103 (2007).
[5] Q. Zhang, Y. Cui, and E. Wang, First-principles approaches to simulate lithiation in silicon electrodes, Modell. Simul. Mater. Sci. Eng. **21**, 074001 (2013).
[6] B. M. Way and J. R. Dahn, The effect of boron substitution in carbon on the intercalation of lithium in $\mathrm{Li}_x(\mathrm{B}_z\mathrm{C}_{1-z})_6$, J. Electrochem. Soc. **141**, 907 (1994).
[7] U. Tanaka, T. Sogabe, H. Sakagoshi, M. Ito, and T. Tojo, Anode property of boron-doped graphite materials for rechargeable lithium-ion batteries, Carbon **39**, 931 (2001).
[8] M. K. Song and K. T. No, Substitution effect of carbon with group 13, 14, and 15 elements on lithium intercalation in graphite, J. Electrochem. Soc. **151**, A1696 (2004).
[9] X. Wang, Z. Zeng, H. Ahn, and G. Wang, First-principles study on the enhancement of lithium storage capacity in boron doped graphene, Appl. Phys. Lett. **95**, 183103 (2009).
[10] Z.-S. Wu, W. Ren, L. Xu, F. Li, and H.-M. Cheng, Doped graphene sheets as anode materials with superhigh rate and large capacity for lithium ion batteries, ACS Nano **5**, 5463 (2011).
[11] E. Rodríguez, I. Cameán, R. García, and A. B. García, Graphitized boron-doped carbon foams: Performance as anodes in lithium-ion batteries, Electrochim. Acta **56**, 5090 (2011).
[12] Z. Zhou, X. Gao, J. Yan, D. Song, and M. Morinaga, A first-principles study of lithium absorption in boron- or nitrogen-doped single-walled carbon nanotubes, Carbon **42**, 2677 (2004).
[13] A. L. M. Reddy, A. Srivastava, S. R. Gowda, H. Gullapalli, M. Dubey, and P. M. Ajayan, Synthesis of nitrogen-doped graphene films for lithium battery application, ACS Nano **4**, 6337 (2010).
[14] E. Pollak, B. Geng, K.-J. Jeon, I. T. Lucas, T. J. Richardson, F. Wang, and R. Kostecki, The interaction of Li+ with single-layer and few-layer graphene, Nano Lett. **10**, 3386 (2010).
[15] L.-J. Zhou, Z. F. Hou, and L.-M. Wu, First-principles study of lithium adsorption and diffusion on graphene with point defects, J. Phys. Chem. C **116**, 21780 (2012).
[16] E. Lee and K. A. Persson, Li absorption and intercalation in single layer graphene and few layer graphene by first principles, Nano Lett. **12**, 4624 (2012).
[17] D. Datta, J. Li, N. Koratkar, and V. B. Shenoy, Enhanced lithiation in defective graphene, Carbon **80**, 305 (2014).
[18] Y. Okamoto, Density functional theory calculations of lithium adsorption and insertion to defect-free and defective graphene, J. Phys. Chem. C **120**, 14009 (2016).
[19] H. Terrones, R. Lv, M. Terrones, and M. S. Dresselhaus, The role of defects and doping in 2d graphene sheets and 1d nanoribbons, Rep. Prog. Phys. **75**, 062501 (2012).
[20] G. Wang, X. Shen, J. Yao, and J. Park, Graphene nanosheets for enhanced lithium storage in lithium ion batteries, Carbon **47**, 2049 (2009).
[21] D. Pan, S. Wang, B. Zhao, M. Wu, H. Zhang, Y. Wang, and Z. Jiao, Li storage properties of disordered graphene nanosheets, Chem. Mater. **21**, 3136 (2009).
[22] S. Yin, Y. Zhang, J. Kong, C. Zou, C. M. Li, X. Lu, J. Ma, F. Y. C. Boey, and X. Chen, Assembly of graphene sheets into hierarchical structures for high-performance energy storage, ACS Nano **5**, 3831 (2011).
[23] R. Mukherjee, A. V. Thomas, D. Datta, E. Singh, J. Li, O. Eksik, V. B. Shenoy, and N. Koratkar, Defect-induced plating of lithium metal within porous graphene networks, Nat. Commun. **5**, 3710 (2014).
[24] J. C. Meyer, C. Kisielowski, R. Erni, M. D. Rossell, M. F. Crommie, and A. Zettl, Direct imaging of lattice atoms and topological defects in graphene membranes, Nano Lett. **8**, 3582 (2008).
[25] F. Banhart, J. Kotakoski, and A. V. Krasheninnikov, Structural defects in graphene, ACS Nano **5**, 26 (2011).
[26] A. T. Balaban, Carbon and its nets, Comput. Math. Appl. **17**, 397 (1989).
[27] X. Rocquefelte, G.-M. Rignanese, V. Meunier, H. Terrones, M. Terrones, and J.-C. Charlier, How to identify haeckelite structures: A theoretical study of their electronic and vibrational properties, Nano Lett. **4**, 805 (2004).
[28] G. Brunetto, P. A. S. Autreto, L. D. Machado, B. I. Santos, R. P. B. dos Santos, and D. S. Galvão, Nonzero gap two-dimensional carbon allotrope from porous graphene, J. Phys. Chem. C **116**, 12810 (2012).
[29] Y.-X. Yu, Graphenylene: a promising anode material for lithium-ion batteries with high mobility and storage, J. Mater. Chem. A **1**, 13559 (2013).
[30] B. Mandal, S. Sarkar, A. Pramanik, and P. Sarkar, Theoretical prediction of a new two-dimensional carbon allotrope and NDR behaviour of its one-dimensional derivatives, Phys. Chem. Chem. Phys. **15**, 21001 (2013).
[31] C. Su, H. Jiang, and J. Feng, Two-dimensional carbon allotrope with strong electronic anisotropy, Phys. Rev. B **87**, 075453 (2013).
[32] B. R. Sharma, A. Manjanath, and A. K. Singh, Pentahexoctite: A new two-dimensional allotrope of carbon, Sci. Rep. **4**, 7164 (2014).

[33] F. Schlütter, T. Nishiuchi, V. Enkelmann, and K. Müllen, Octafunctionalized biphenylenes: Molecular precursors for isomeric graphene nanostructures, Angew. Chem., Int. Ed. **53**, 1538 (2014).

[34] H. J. Hwang, J. Koo, M. Park, N. Park, Y. Kwon, and H. Lee, Multilayer graphynes for lithium ion battery anode, J. Phys. Chem. C **117**, 6919 (2013).

[35] H. Zhang, Y. Xia, H. Bu, X. Wang, M. Zhang, Y. Luo, and M. Zhao, Graphdiyne: A promising anode material for lithium ion batteries with high capacity and rate capability, J. Appl. Phys. **113**, 044309 (2013).

[36] The calculation was based on a CR2032 $LiMnO_2$ coin cell battery of 20 mm diameter containing 0.1088 g of graphite converted to the equivalent mass in terms of graphene surface.

[37] A. K. Geim and I. V. Grigorieva, van der waals heterostructures, Nature (London) **499**, 419 (2013).

[38] P. Iqbal, J. A. Preece, and P. M. Mendes, Nanotechnology: The top-down and bottom-up approaches, in *Supramolecular Chemistry* (John Wiley & Sons, Ltd., New York, 2012).

[39] J. W. Colson and W. R. Dichtel, Rationally synthesized two-dimensional polymers, Nat. Chem. **5**, 453 (2013).

[40] J.-J. Adjizian, P. Briddon, B. Humbert, J.-L. Duvail, P. Wagner, C. Adda, and C. Ewels, Dirac cones in two-dimensional conjugated polymer networks, Nat. Commun. **5**, 5842 (2014).

[41] J.-J. Adjizian, A. Lherbier, S. M.-M. Duboi, A. R. Botello-Mendez, and J.-C. Charlier, The electronic and transport properties of two-dimensional conjugated polymer networks including disorder, Nanoscale **8**, 1642 (2016).

[42] K. Persson, Y. Hinuma, Y. S. Meng, A. Van der Ven, and G. Ceder, Thermodynamic and kinetic properties of the Li-graphite system from first-principles calculations, Phys. Rev. B **82**, 125416 (2010).

[43] E. Hazrati, G. A. de Wij, and G. Brocks, Li intercalation in graphite: A van der Waals density-functional study, Phys. Rev. B **90**, 155448 (2014).

[44] V. H. Crespi, L. X. Benedict, M. L. Cohen, and S. G. Louie, Prediction of a pure-carbon planar covalent metal, Phys. Rev. B **53**, R13303 (1996).

[45] G. Kresse and J. Furthmüller, Efficiency of ab-initio total energy calculations for metals and semiconductors using a plane-wave basis set, Comput. Mater. Sci. **6**, 15 (1996).

[46] G. Kresse and J. Furthmüller, Efficient iterative schemes for ab initio total-energy calculations using a plane-wave basis set, Phys. Rev. B **54**, 11169 (1996).

[47] J. Klimeš, D. R. Bowler, and A. Michaelides, van der Waals density functionals applied to solids, Phys. Rev. B **83**, 195131 (2011).

[48] J. Klimeš, D. R Bowler, and A. Michaelides, Chemical accuracy for the van der Waals density functional, J. Phys.: Condens. Matter **22**, 022201 (2010).

[49] G. Román-Pérez and J. M. Soler, Efficient Implementation of a van der Waals Density Functional: Application to Double-Wall Carbon Nanotubes, Phys. Rev. Lett. **103**, 096102 (2009).

[50] M. Dion, H. Rydberg, E. Schröder, D. C. Langreth, and B. I. Lundqvist, van der Waals Density Functional for General Geometries, Phys. Rev. Lett. **92**, 246401 (2004).

[51] H. Rydberg, B. I. Lundqvist, D. C. Langreth, and M. Dion, Tractable nonlocal correlation density functionals for flat surfaces and slabs, Phys. Rev. B **62**, 6997 (2000).

[52] H. Rydberg, M. Dion, N. Jacobson, E. Schröder, P. Hyldgaard, S. I. Simak, D. C. Langreth, and B. I. Lundqvist, van der Waals Density Functional for Layered Structures, Phys. Rev. Lett. **91**, 126402 (2003).

[53] P. E. Blöchl, Projector augmented-wave method, Phys. Rev. B **50**, 17953 (1994).

[54] G. Kresse and D. Joubert, From ultrasoft pseudopotentials to the projector augmented-wave method, Phys. Rev. B **59**, 1758 (1999).

[55] H. J. Monkhorst and J. D. Pack, Special points for Brillouin-zone integrations, Phys. Rev. B **13**, 5188 (1976).

[56] S. P. Ong, W. D. Richards, A. Jain, G. Hautier, M. Kocher, S. Cholia, D. Gunter, V. L. Chevrier, K. A. Persson, and G. Ceder, Python materials genomics (pymatgen): A robust, open-source python library for materials analysis, Comput. Mater. Sci. **68**, 314 (2013).

[57] R. F. W. Bader, *Atoms in Molecules: A Quantum Theory* (Oxford University Press, Oxford, 1994).

[58] G. Henkelman, A. Arnaldsson, and H. Jónsson, A fast and robust algorithm for Bader decomposition of charge density, Comput. Mater. Sci. **36**, 354 (2006).

[59] X. Gonze, F. Jollet, F. A. Araujo, D. Adams, B. Amadon, T. Applencourt, C. Audouze, J.-M. Beuken, J. Bieder, A. Bokhanchuk, E. Bousquet, F. Bruneval, D. Caliste, M. Côté, F. Dahm, F. D. Pieve, M. Delaveau, M. D. Gennaro, B. Dorado, C. Espejo, G. Geneste, L. Genovese, A. Gerossier, M. Giantomassi, Y. Gillet, D. R. Hamann, L. He, G. Jomard, J. L. Janssen, S. Le Roux, A. Levitt, A. Lherbier, F. Liu, I. Lukačević, A. Martin, C. Martins, M. J. T. Oliveira, S. Poncé, Y. Pouillon, T. Rangel, G.-M. Rignanese, A. H. Romero, B. Rousseau, O. Rubel, A. A. Shukri, M. Stankovski, M. Torrent, M. J. V. Setten, B. V. Troeye, M. J. Verstraete, D. Waroquiers, J. Wiktor, B. Xu, A. Zhou, and J. W. Zwanziger, Recent developments in the ABINIT software package, Comput. Phys. Commun. **205**, 106 (2016).

[60] R. M. Martin, *Electronic Structure, Basic Theory and Practical Methods* (Cambridge University Press, Cambridge, UK, 2004).

[61] J. P. Perdew, K. Burke, and M. Ernzerhof, Generalized Gradient Approximation Made Simple, Phys. Rev. Lett. **77**, 3865 (1996).

[62] S. Grimme, Semiempirical GGA-type density functional constructed with a long-range dispersion correction, J. Comput. Chem. **27**, 1787 (2006).

[63] S. Grimme, J. Anthony, S. Ehrlich, and H. Krieg, A consistent and accurate ab initio parametrization of density functional dispersion correction (DFT-D) for the 94 elements H-Pu, J. Chem. Phys. **132**, 154104 (2010).

[64] S. Grimme, S. Ehrlich, and L. Goerigk, Effect of the damping function in dispersion corrected density functional theory, J. Comput. Chem. **32**, 1456 (2010).

[65] B. Van Troeye, M. Torrent, and X. Gonze, Interatomic force constants including the DFT-D dispersion contribution, Phys. Rev. B **93**, 144304 (2016).

[66] D. R. Hamann, Optimized norm-conserving Vanderbilt pseudopotentials, Phys. Rev. B **88**, 085117 (2013).

[67] J. M. Soler, E. Artacho, J. D. Gale, A. García, J. Junquera, P. Ordejón, and D. Sánchez-Portal, The SIESTA method for *ab initio* order-*N* materials simulation, J. Phys.: Condens. Matter **14**, 2745 (2002).

[68] A. R. Botello-Méndez, S. M.-M. Dubois, A. Lherbier, and J.-C. Charlier, Achievements of DFT for the investigation of

graphene-related nanostructures, Acc. Chem. Res. **47**, 3292 (2014).

[69] R. Zacharia, H. Ulbricht, and T. Hertel, Interlayer cohesive energy of graphite from thermal desorption of polyaromatic hydrocarbons, Phys. Rev. B **69**, 155406 (2004).

[70] Y. Imai and A. Watanabe, Energetic evaluation of possible stacking structures of Li-intercalation in graphite using a first-principle pseudopotential calculation, J. Alloys Compd. **439**, 258 (2007).

[71] Y. Liu, V. I. Artyukhov, M. Liu, A. R. Harutyunyan, and B. I. Yakobson, Feasibility of lithium storage on graphene and its derivatives, J. Phys. Chem. Lett. **4**, 1737 (2013).

[72] N. Takami, A. Satoh, M. Hara, and T. Ohsaki, Structural and kinetic characterization of lithium intercalation into carbon anodes for secondary lithium batteries, J. Electrochem. Soc. **142**, 371 (1995).

[73] J. Hermann, R. A. DiStasio, and A. Tkatchenko, First-principles models for van der Waals interactions in molecules and materials: Concepts, theory, and applications, Chem. Rev. **117**, 4714 (2017).

[74] W. J. Kim, M. Kim, E. K. Lee, S. Lebègue, and H. Kim, Failure of density functional dispersion correction in metallic systems and its possible solution using a modified many-body dispersion correction, J. Phys. Chem. Lett. **7**, 3278 (2016).

[75] J. Park, B. D. Yu, and S. Hong, van der Waals density functional theory study for bulk solids with bcc, fcc, and diamond structures, Curr. Appl. Phys. **15**, 885 (2015).

[76] Y. Baskin and L. Meyer, Lattice constants of graphite at low temperatures, Phys. Rev. **100**, 544 (1955).

[77] V. V. Avdeev, A. P. Savchenkova, L. A. Monyakina, I. V. Nikol'skaya, and A. V. Khvostov, Intercalation reactions and carbide formation in graphite-lithium system, J. Phys. Chem. Solids **57**, 947 (1996).

[78] D. Ferguson, D. J. Searles, and M. Hankel, Biphenylene and phagraphene as lithium ion battery anode materials, ACS Appl. Mater. Interfaces **9**, 20577 (2017).

[79] F. Yao, F. Güneş, H. Q. Ta, S. M. Lee, S. J. Chae, K. Y. Sheem, C. S. Cojocaru, S. S. Xie, and Y. H. Lee, Diffusion mechanism of lithium ion through basal plane of layered graphene, J. Am. Chem. Soc. **134**, 8646 (2012).

[80] X. Fan, W. T. Zheng, and J.-L. Kuo, Adsorption and diffusion of Li on pristine and defective graphene, ACS Appl. Mater. Interfaces **4**, 2432 (2012).

[81] D. Das, S. Kim, K.-R. Lee, and A. K. Singh, Li diffusion through doped and defected graphene, Phys. Chem. Chem. Phys. **15**, 15128 (2013).

[82] P. Verma, P. Maire, and P. Novák, A review of the features and analyses of the solid electrolyte interphase in Li-ion batteries, Electrochim. Acta **55**, 6332 (2010).

[83] S. J. An, J. Li, C. Daniel, D. Mohanty, S. Nagpure, and D. L. Wood, The state of understanding of the lithium-ion-battery graphite solid electrolyte interphase (SEI) and its relationship to formation cycling, Carbon **105**, 52 (2016).

[84] Y. Wen, K. He, Y. Zhu, F. Han, Y. Xu, I. Matsuda, Y. Ishii, J. Cumings, and C. Wang, Expanded graphite as superior anode for sodium-ion batteries, Nat. Commun. **5**, 4033 (2014).

[85] Y. Liu, B. V. Merinov, and W. A. Goddard, Origin of low sodium capacity in graphite and generally weak substrate binding of Na and Mg among alkali and alkaline earth metals, Proc. Natl. Acad. Sci. U.S.A. **113**, 3735 (2016).